Astronomy & Astrophysics manuscript no. example
September 13, 2023

arXiv:2309.06266v1 [astro-ph.SR] 12 Sep 2023

Modelling the interaction of Alfvénic fluctuations with coronal mass ejections in the low solar corona

Chaitanya Prasad Sishtla[1], Jens Pomoell[1], Rami Vainio[2], Emilia Kilpua[1], and Simon Good[1]

[1] Department of Physics, University of Helsinki, Helsinki, Finland
e-mail: `chaitanya.sishtla@helsinki.fi`
[2] Department of Physics & Astronomy, University of Turku, Turku, Finland

ABSTRACT

Context. Alfvénic fluctuations of various scales are ubiquitous in the corona, with their non-linear interactions and eventual turbulent cascade resulting in an important heating mechanism that accelerates the solar wind. These fluctuations may be processed by large-scale, transient and coherent heliopsheric structures such as coronal mass ejections (CMEs). In this study we investigate the interactions between Alfvénic solar wind fluctuations and CMEs using MHD simulations.

Aims. We study the transmission of upstream solar wind fluctuations into the CME leading to the formation of CME sheath fluctuations. Additionally, we investigate the influence of the fluctuation frequencies on the extent of the CME sheath.

Methods. We use an ideal magnetohydrodynamic (MHD) model with an adiabatic equation of state. An Alfvén pump wave is injected into the quiet solar wind by perturbing the transverse magnetic field and velocity components, and a CME is injected by inserting a flux-rope modelled as a magnetic island into the quasi-steady solar wind.

Results. The upstream Alfvén waves experience a decrease in wavelength and change in the wave vector direction due to the non-radial topology of the CME shock front. The CME sheath inhibits the transmission of high wavelength fluctuations due to the presence of non-radial flows in this region. The frequency of the solar wind fluctuations also affects the steepening of MHD fast waves causing the CME shock propagation speed to vary with the solar wind fluctuation frequencies.

Key words. coronal mass ejections (CMEs), Alfvén waves, MHD,

1. Introduction

The turbulent fluctuations in velocity, magnetic field, electric field, and density are ubiquitous in the solar wind and corona (Coleman Jr 1968; Belcher & Davis Jr 1971; Bale et al. 2005). The convective motions of the dense photospheric plasma, containing the solar magnetic field, are considered to be the primary source of energy for these fluctuations (Cranmer & Van Ballegooijen 2005; Kato et al. 2016). These fluctuations have been observed both in-situ (Belcher & Davis Jr 1971; D'Amicis & Bruno 2015) and remotely (Tomczyk et al. 2007). In the solar wind, the power contained in Alfvénically polarised fluctuations dominates over the power in compressive fluctuations (Tu & Marsch 1995; Chen 2016). Additionally, the solar wind exhibits broad-band Alfvénic fluctuations, which can then nonlinearly interact to initiate an energy cascade leading to dissipation via heating at smaller spatial scales. In this view of a turbulence cascade, the inertial range is the spatial scale of the fluctuations exhibiting a power law behaviour between the energy injection and dissipation scales. This inertial-range turbulence is often studied within the framework of reduced magnetohydrodynamics (RMHD), in which Alfvén waves are the linear wave modes (Zank & Matthaeus 1992; Schekochihin et al. 2009; Perez & Chandran 2013). Previous studies (Matthaeus et al. 1984; Gershman et al. 2019; González et al. 2021) have also discussed the role of Alfvén wave propagation and reflection-driven Alfvénic turbulence for particle acceleration in planetary radiation belts, MHD reconnection sites, and at interplanetary discontinuities.

In this study, we investigate the interaction of Alfvénic perturbations with a coronal mass ejection (CME) in the low corona. A CME is a transient plasma and magnetic field eruption from the solar corona and exhibits complex magnetic substructures. They are one of the primary drivers of geomagnetic activity near Earth (Kilpua et al. 2013, 2015; Kalliokoski et al. 2020, 2022). In coronagraph images, CMEs often exhibit a three-part structure with a bright loop of compressed coronal plasma enclosing a dark, low-density cavity (corresponding to a flux rope), which contains a high-density core (Gibson & Low 2000; Kilpua et al. 2017b). A spacecraft encountering a CME typically observes a shock, followed by a turbulent sheath and the ejecta. Only part of the ejecta at 1 AU shows clear flux rope signatures due to interaction and evolution. The internal structure of the CME is of significant interest as flux ropes can cause strong and sustained southward magnetic fields influencing the Earth (Kilpua et al. 2017a). In addition, the turbulent and compressed CME sheath is highly geoeffective (Kilpua et al. 2017b, 2019). Sheaths are known to exhibit an extensive range of inertial and kinetic range spectral indices (Kilpua et al. 2020, 2021), embed multi-scale structures (Ruohotie et al. 2022) and contribute to the acceleration of solar energetic particles (Kilpua et al. 2021). The fluctuations in the CME sheath have been seen to exhibit turbulence characteristics often observed in the slow solar wind (e.g. higher compressibility), yet they are still dominated by non-compressible Alfvénic fluctuations (Moissard et al. 2019). Additionally, compared to the predominantly anti-sunward fluctuations in the solar wind preceding CMEs near 1 AU, sheaths are found to exhibit a more balanced distribution of sunward and anti-sunward fluctuations (Good et al. 2020; Good et al. 2022; Soljento et al. 2023). There is currently a wide range of models (Gibson & Low 1998; Isavnin 2016; Verbeke et al. 2019; Asvestari et al. 2021, 2022) to investigate the evolution of the global flux rope structure of CMEs from Sun to Earth and their interactions with the ambient solar wind. However, we need the understanding and capabilities to model the smaller-scale features of CMEs and their sheath regions. One important aspect is the transmission of Alfvénic fluctuations from the surrounding ambient solar wind into the CME and the role it plays in forming the sheath.

In this study, by using numerical simulations, we aim to enhance our understanding of the formation of sheath structures by demonstrating the effect of Alfvénic solar wind fluctuations on the large-scale structures of the CME and to analyse the transmission of these fluctuations into the sheath region. We find the CME shock speed influenced by the frequency of solar wind fluctuations, with the CME sheath exhibiting non-radial flows, along with both sunward and anti-sunward Alfvénic fluctuations. These results are obtained by performing 2.5D MHD simulations of the solar corona assuming a radial solar magnetic field, with the flux rope modelled using the Grad-Shafranov equation.

In Section 2, we introduce the MHD equations and associated boundary conditions, the mechanism for Alfvén wave injection, and the CME model used for the simulations. The influence of solar wind fluctuations on the CME and their transmission to the sheath is discussed in Section 3. Section 4 presents a statistical comparison of the shock location and sheath extent for varying solar wind and CME parameters, including a case with no solar wind fluctuations. The conclusions are summarised in Section 5.

2. Methodology

To perform our study, we developed a 2.5D magnetohydrodynamic (MHD) simulation from the low corona at 1.03 solar radii ($R_\odot$) to 30 $R_\odot$. The simulation domain is 2D in space with velocity and electromagnetic field vectors having three components. The solar wind is modelled assuming a global radial unipolar (outward) solar magnetic field which can be considered realistic for a limited region of the Sun such as a coronal hole. The MHD equations and the relevant physical processes of gravity and ad-hoc coronal heating are described by the following equations:

$$\frac{\partial \rho}{\partial t} + \nabla \cdot (\rho \mathbf{v}) = 0 \tag{1}$$

$$\frac{\partial (\rho \mathbf{v})}{\partial t} + \nabla \cdot [\rho \mathbf{v}\mathbf{v} + (P + \frac{B^2}{2\mu_0})\mathbf{I} - \frac{\mathbf{B}\mathbf{B}}{\mu_0}] = -\frac{GM_\odot \rho}{r^2}\hat{\mathbf{r}} \tag{2}$$

$$\frac{\partial \mathcal{E}}{\partial t} + \nabla \cdot [(\mathcal{E} + P - \frac{B^2}{2\mu_0})\mathbf{v} + \frac{1}{\mu_0}\mathbf{B} \times (\mathbf{v} \times \mathbf{B})] = -\frac{GM_\odot \rho v_r}{r^2} + S \tag{3}$$

$$\nabla \cdot \mathbf{B} = 0 \tag{4}$$

$$\frac{\partial \mathbf{B}}{\partial t} - \nabla \times (\mathbf{v} \times \mathbf{B}) = 0 \tag{5}$$

where

$$\mathcal{E} = \frac{1}{2}\rho v^2 + \frac{P}{\gamma - 1} + \frac{B^2}{2\mu_0}, \tag{6}$$

$$S = S_0 \exp\left(-\frac{r}{L}\right). \tag{7}$$

Here the quantities ρ, $\mathbf{v}$, $\mathbf{B}$, $\mathcal{E}$, and P correspond to the mass density, bulk plasma velocity, magnetic field, total energy density, and thermal pressure. Equations 1-5 correspond to the mass continuity, momentum, energy continuity, and induction equations, respectively, and will subsequently be referred to as such. The solar wind plasma evolves by solving these MHD equations for an adiabatic polytropic index of $\gamma = 5/3$. Thus, to obtain a steady-state solar wind that approximates a Parker-like outflow, we incorporate an additional energy source term in Equation 7 (Pomoell et al. 2015; Mikić et al. 2018; Sishtla et al. 2022) with $S_0 = 0.5 \times 10^{-6}$ Wm^{-3} and $L = 0.4\, R_\odot$.

The numerical method used in this work to solve the MHD equations has been employed in previous studies of the solar corona (Pomoell & Vainio 2012). The method utilises a strong stability preserving (SSP) Runge-Kutta method to advance the semi-discretised equations in time, and employs the Harten–Lax–van Leer (HLL) approximate Riemann solver supplied by piece-wise, linear slope-limited interface states. The equations are solved in spherical coordinates and the magnetic field is ensured to be divergence free to the floating point accuracy by utilising the constrained transport method (Kissmann & Pomoell 2012).

The MHD equations are integrated forward in time for a 2D meridional plane with a radial extent of $r = r_0 = 1.03\, R_\odot$ to $r = 30\, R_\odot$, and an co-latitudinal extent of $\theta = 10°$ to $\theta = 170°$. The domain is, therefore, symmetric in the out-of-plane longitudinal ϕ direction. The solar magnetic field is initialised to be radially outwards with an associated vector potential $\mathbf{A} = -B_0 r_0 (r_0/r) \cot\theta\, \hat{\phi}$ where $B_0 = 5$ G, and the magnetic field in the simulation is then specified using $\mathbf{B} = \nabla \times \mathbf{A}$. The simulation grid is defined by 500 cells logarithmically spaced in the radial direction, and 128 equidistant cells in the latitudinal direction. Appendix A validates this choice of the radial grid resolution by verifying the results presented in the following sections for a significantly higher resolution.

At the inner radial boundary, representing the coronal base, we specify a constant mass density and temperature along the boundary with $\rho_0 = 8.5 \times 10^{-13}$ kg and $T_0 = 1.2 \times 10^6$ K. At the outer radial and the latitudinal boundaries, we linearly extrapolate all dynamical quantities to enforce an outflow boundary condition.

2.1. Introducing Alfvénic perturbations

After achieving a steady-state solar wind by integrating Equations 1- 7 in time, we introduce Alfvénic fluctuations. The Alfvén waves are introduced at the coronal base by utilising a time-dependent boundary condition for the Elsässer variables, defined by

$$\mathbf{z}_\perp^\pm = \mathbf{v}_\perp \pm \frac{\mathbf{B}_\perp}{\sqrt{\mu_0 \rho}}. \tag{8}$$

We continuously inject the monochromatic and linearly polarized Alfvénic fluctuations in the out-of-plane ϕ direction by specifying the anti-sunward (outgoing) Elsässer variable as $\delta \mathbf{z}^- = \mathrm{Z}_0 \sin(2\pi f_0 t)\, \hat{\phi}$ at the lower boundary with $\mathrm{Z}_0 = 32\sqrt{2}$ kms^{-1} being the amplitude and f_0 the frequency of the wave.

In Figure 1 we present the quasi-steady solar wind after the injection of a 3 mHz Alfvén wave. In general, the solar wind response to the injected fluctuations depends on the polarization of the waves (Goldstein 1978; Hollweg 1971). The propagation of the linearly polarised injected Alfvén wave causes a fluctuating magnetic field strength which results in the steepening of

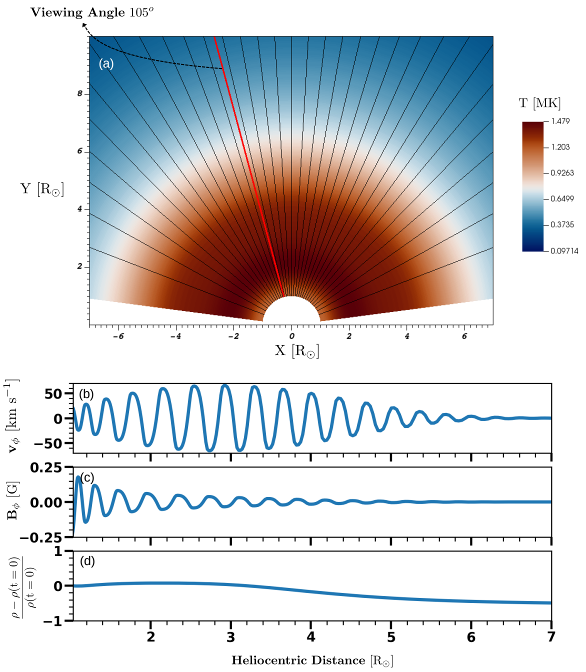

Fig. 1. Coronal quasi-steady state. Panel (a) shows a snapshot of the plasma temperature upon the injection of a 3 mHz linearly polarised Alfvén wave, with an annotation describing the viewing angle along 105°. In panels (b) and (c), we present the out-of-plane v_ϕ velocity and B_ϕ magnetic field components along the viewing angle. The variations in the density ρ from the quasi-steady values prior to the injection of the Alfvén wave are presented in panel (d).

the Alfvén waves themselves (Cohen & Kulsrud 1974), in addition to generating density fluctuations due to the ponderomotive force (Nakariakov et al. 1997). Due to this in Figure 1(a) we observe an increase in temperature from 1.2 MK at the lower boundary to 1.4 MK near 3 $R_\odot$, before decreasing again. The generation of density fluctuations is a second-order non-linear effect and is absent in incompressible MHD. In this simulation the density fluctuations are absent as the chosen grid resolution causes the Alfvén waves to be damped due to numerical diffusion before the density fluctuations can be generated. This damping ensures we only have a pure monochromatic Alfvén wave in the simulation which does not yet experience any reflections from large-scale density gradients in the solar wind (Verdini & Velli 2007; Van Ballegooijen et al. 2011), and confines the waves to be present below ≈ 10 R$_\odot$. Thus, in this study we confine our analysis to the wind below ≈ 10 R$_\odot$.

The Alfvénicity, steepening, and absence of density fluctuations in the simulation are illustrated by considering the radial propagation of the injected waves along a viewing angle (annotated in Figure 1(a)). In Figure 1(b), (c) we present the out-of-plane velocity v_ϕ and magnetic field B_ϕ components along this viewing angle. Upon comparing the two panels, we observe an anti-correlation between v_ϕ and B_ϕ which confirms both the Alfvénicity and anti-sunward direction of the injected wave. Furthermore, to verify the lack of accompanying density perturbations, we plot in Figure 1(d) the fluctuating component of the mass density $\Delta\rho/\rho = (\rho - \rho(t = 0))/\rho(t = 0)$ where $\rho(t = 0)$ is the mass density in the coronal volume prior to the Alfvén wave injection. The panel shows a large-scale variation in the density, but the absence of any smaller-scale fluctuations.

2.2. Introducing a Coronal Mass Ejection

In this study, we don't model the initiation and subsequent eruption of the CME but instead directly instantiate an erupting plasma structure mimicking an eruptive CME. We superimpose an appropriate plasma structure on the quasi-steady solar wind containing the Alfvénic fluctuations to achieve this.

The magnetic field of the CME is modelled as a force-free flux rope (FR) using the Soloviev solution of the Grad-Shafranov (GS) equation (Solov'ev 1968). The solutions to the GS equation represent axisymmetric MHD equilibria of magnetized plasmas without flows such that the equilibrium condition

$$\mathbf{J} \times \mathbf{B} = \nabla P \tag{9}$$

is satisfied where $\mathbf{J}$ is the current density given by $\mathbf{J} = \nabla \times \mathbf{B}/\mu_0$, and P is the thermal pressure of the plasma. Once the magnetic structure of the CME is modelled using Equation 9 under the assumption of zero-beta ($P = 0$) conditions we then populate it with plasma to model a high density ejecta. The density inside the structure is specified as

$$\rho_{\text{cme}} = \frac{\rho_{\text{cme},0}}{2}\left[1 - \cos\left(\pi\frac{d_{\text{cme}} - d}{d_{\text{cme}}}\right)\right], \tag{10}$$

where d is the distance from the centre of the structure and d_{cme} is the radial extent, and $\rho_{\text{cme},0}$ is the density specified at the centre. This formulation of ρ_{cme} ensures a continuous transition from the high density $\rho_{\text{cme},0}$ CME core to the background density at the edge of the structure. We also initialise the plasma with a constant temperature of 0.5×10^6 K, and an ejection velocity $\mathbf{v}_{\text{ej}}$ along the radial direction inside the CME. The constructed CME (Equations 9, 10) is then superimposed on the quasi-steady solar wind including the Alfvénic fluctuations described in Section 2.1. We note that due to the ad-hoc specification of the thermal pressure inside the CME and superposition of the structure on the quasi-steady wind the plasma in and immediately surrounding the CME is not in equilibrium causing the FR to expand and propagate.

In Figure 2 we present a schematic showing the magnetic field configuration and dynamic contributions acting on the CME at the onset. The poloidal field of the FRs we use for this study is oriented in the anti-clockwise direction as seen by the direction of magnetic field vectors around the FR. This causes them to deflect when reconnecting with the radially outward magnetic field lines. The ejection velocity is additionally directed in the radial direction.

The plasma signatures encountered by a virtual spacecraft upon traversing such an FR are shown in Figure 3 with dashed vertical lines demarcating the upstream, CME sheath, and FR regions. The spacecraft is placed at 5 $R_\odot$, and a viewing angle of 105 degrees with the time axis referenced from the time of CME injection in the simulation. The CME is modelled using an initial speed $v_{\text{ej}} = 500$ km s^{-1}, peak density of $2\rho_0$ (ρ_0 is the constant mass density at the coronal base at $r = r_0$), and $B_\phi \approx 12$ G. Prior to encountering the CME, the virtual spacecraft measures the pristine upstream solar wind conditions as seen in Figures 3(a)-(d). We observe anti-sunward Alfvénic fluctuations by the anti-correlated variations in B_ϕ and v_ϕ. The first CME-related signature registered is the shock at $t \approx 15$ mins. The shock is followed by the CME sheath. In this sheath region, we observe larger non-radial flows (as compared to the upstream fluctuations) as non-zero values for v_θ and v_ϕ (Figure 3(b)). The CME sheath is also characterised by an enhanced density and temperature (Figures 3(c), (d)) due to the shock transition and plasma piling ahead of the CME. Finally, the spacecraft encounters the FR.

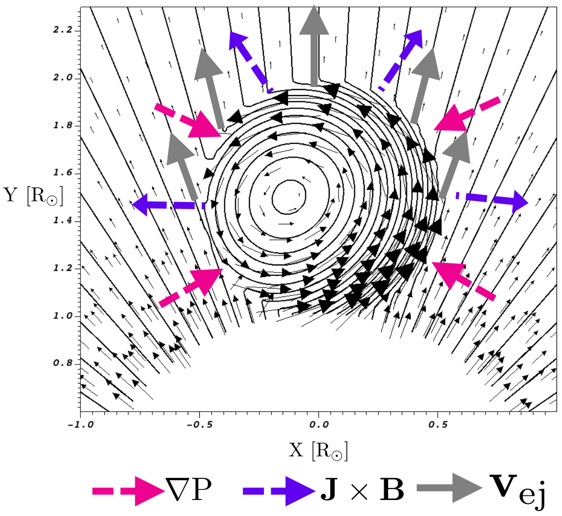

Fig. 2. CME insertion into the solar wind.The black curves show magnetic field lines with the black arrows indicating the direction and relative strength. The figure is annotated with the directions of the ∇P and $\mathbf{J} \times \mathbf{B}$ forces that comprise the Grad-Shafranov equilibrium condition. An initial ejection velocity $\mathbf{v}_{\rm ej}$ is given to the CME along the radial direction.

It is featured by a smooth variation of B_θ (Figure 3(a)) indicating rotation of the field as it crosses the magnetic island initialised in Equation 9. The FR region has also a relatively high density (Figure 3(c)).

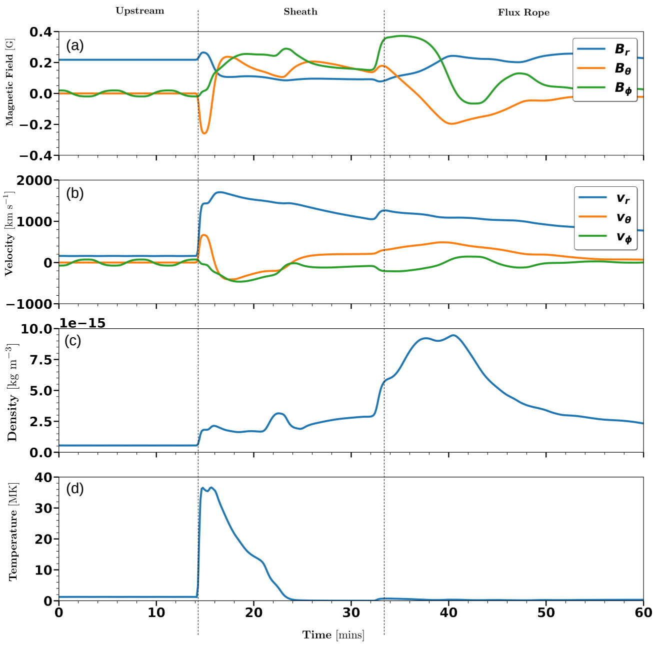

Fig. 3. CME encounter with virtual spacecraft. The by virtual spacecraft is located at 5 $R_\odot$ and a viewing angle of 105°. The vertical lines differentiate the upstream, sheath, and flux rope encountered by the spacecraft.

3. Results

In this Section we describe the interaction of the Alfvénic fluctuations in the quasi-steady solar wind (Section 2.1) with a CME modelled as in Section 2.2 with $v_{\rm ej} = 500$ km s^{-1}, peak density of $2\rho_0$, and $B_\phi \approx 12$ G. The CME is deflected in the -X direction as it reconnects with the anti-sunward-directed radial magnetic field line due to the chosen poloidal field direction of the FR. In Figure 4(a)–(c) we show the density compression ratio computed as $\rho(t)/\rho(t = 0)$ (Pomoell et al. 2015), the plasma beta $\beta = p_{\rm thermal}/p_{\rm magnetic}$, and the out-of-plane (longitudinal) velocity component v_ϕ at simulation time $t = 10.8$ min.

The initial velocity of the FR ($\mathbf{v}_{\rm ej}$) and the out-of-equilibrium $\mathbf{J} \times \mathbf{B} - \nabla P$ force allows the plasma of the CME to expand at a rate much higher than the ambient solar wind velocity. This results in the FR driving a fast mode shock. In an ideal MHD system, the maximum density compression ratio at a shock front is $\frac{\gamma+1}{\gamma-1}$ (e.g., Koskinen 2011) which in our case, with $\gamma = 5/3$, gives a theoretical maximum compression of 4. At the shock front, located approximately at 2.5 $R_\odot$, there is an observed density compression jump from 1 in the upstream region to ≈ 2 inside the sheath at the flank of the CME, and ≈ 3 near the head-on region of the CME. The FR is driving a shock as a result of the large difference between the CME ejection velocity and upstream solar wind velocity. The FR trails behind the leading shock front and is identified by the closed field lines forming the magnetic island. The sheath is the region between the shock and FR. CME sheath regions are often characterised by non-radial flows and buildup of density in a pile-up compression region (PUC) (Das et al. 2011). In our simulation, the presence of non-radial flows is due to the draping of the flow around the magnetic island in the sheath (Siscoe & Odstrcil 2008). This draping causes the formation of an oblique shock, which in turn causes large-scale flows to be generated to maintain the non-radial continuities in the Rankine-Hugoniot jump conditions. Additionally, the compression of plasma in the sheath region causes the formation of a PUC. Figure 4(a) is annotated with markings denoting the PUC, the sheath region, and the location of the reconnection site causing the CME to deflect. The reconnection at the CME flank reduces magnetic flux at this location while the field still drapes around the FR in the opposite flank. This drives a strong magnetic field gradient that deflects the CME.

In Figure 4(b) we plot the plasma beta in the simulation to investigate whether plasma dynamics are dominated by the magnetic field (low β) or gas dynamics (high β). We see that the whole steady state solar wind upstream of the shock has $\beta \ll 1$, which indicates a frozen-in plasma condition is strongly met. We observe a region of high β inside the sheath as we view the CME head-on and around the reconnection site. In comparing with Figure 4(a), we see that this high β region occurs when we encounter a region of enhanced density inside the sheath. The FR is isolated from the surrounding sheath region and maintains a low β.

Finally, in Figure 4(c) and 4(d) we present the v_ϕ and v_θ components in the simulation, respectively. At the CME flanks, we see that the solar wind perturbations in v_ϕ are modified by the shock. The radially directed wave vectors upstream of the shock are modified downstream to reflect the non-radial topology of the shock front. However, in the regions of enhanced β from Figure 4(b), there are significant flows in the $\pm\phi$ directions, as shown by the large v_ϕ magnitudes. These are the non-radial flows that are generated as a result of the structure of the FR that causes the solar magnetic field to drape around it, as well as the strong guide field of the FR affecting the flow of the surrounding

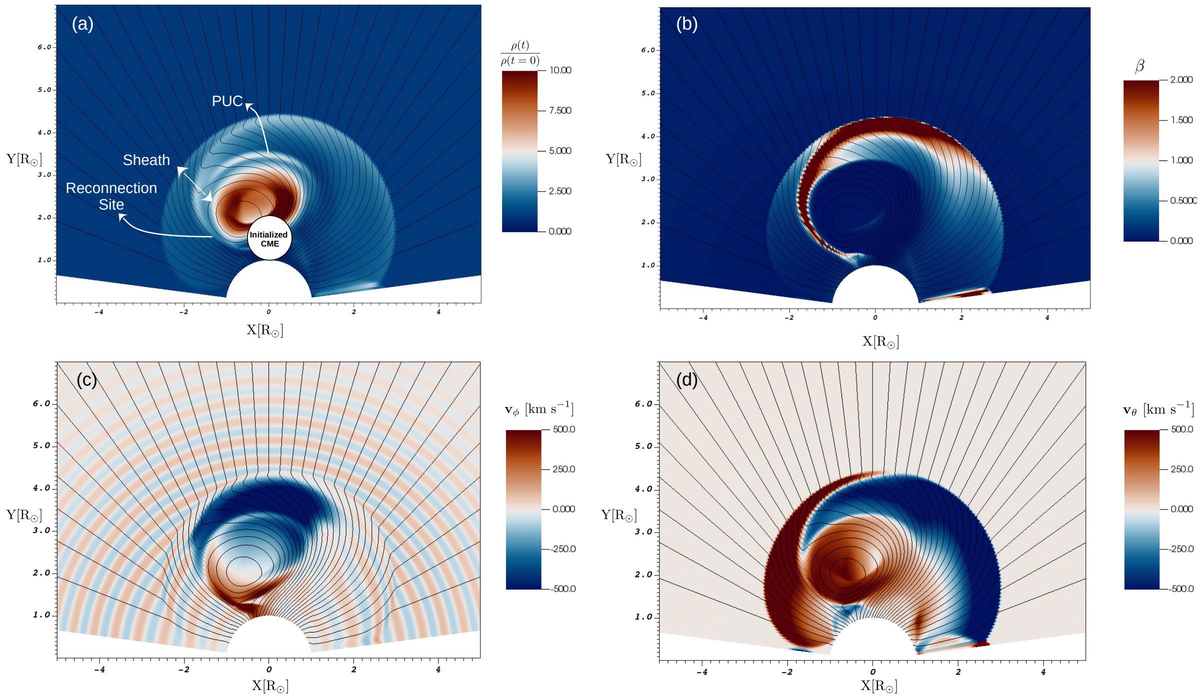

Fig. 4. Snapshots of CME propagation. The figure presents snapshots of the simulation as the CME is propagating in the low corona at $t = 10.8$ mins. In (a) the colour intensity denotes the density compression compared to the quasi-steady solar wind, with annotations indicating the PUC, sheath, and reconnection site. The plot in panel (b) shows the plasma beta, and panels (c), (d) present the out-of-plane velocity component v_ϕ and the co-latitudinal (meridional) component v_θ.

plasma. The spatial extent of the non-radial flows, as depicted by the dark blue region in Figure 4(c), indicates a similarity in size to the wavelength of Alfvén waves at the flanks of the CME. The v_θ component does not have any perturbations upstream as expected. However, downstream of the shock, we see large flows in θ as the FR sweeps away the surrounding plasma as it propagates.

3.1. CME modified solar wind fluctuations

The cut through the CME flanks in Figure 4(c) shows that the frequency of the upstream solar wind fluctuations decreases downstream of the shock. Alfvénic fluctuations such as these are characterised by a correlation in the velocity and magnetic field (Belcher et al. 1969) and can be identified by the accompanying Elsässer variables (Equation 8). Fluctuations can be identified by subtracting the mean plasma flow speed from the accompanying Elsässer variable. The simulation snapshots of the anti-sunward propagating Elsässer variable z_ϕ^- at various times is shown in Figure 5. This figure is annotated with the viewing angle of 160° corresponding to the flank of the CME.

The panels (a) and (b) present the anti-sunward Elsässer variable 6.25 and 8.75 minutes after the onset of the eruptive event, respectively. The significant negative value of z_ϕ^- in the figure is due to the positive B_ϕ inside the flux-rope. The large positive B_ϕ field compresses the plasma ahead of it, causing the large negative valued z_ϕ^-. This positive B_ϕ along with the anti-clockwise direction of the poloidal field around the FR (Figure 2) denotes a positive (right-handed) chirality for the FR. At the flanks, the initially expanding CME amplifies the imposed fluctuations on the flanks as it 'drags' the solar wind at speeds higher than the ambient Alfvén velocity prior to shock formation (Figures 5(a)-(d)). After the formation of a shock along the 160° viewing angle in panel (e), these CME-modified anti-sunward fluctuations are also present in the downstream region.

3.1.1. Shock transmitted solar wind fluctuations

The presence of a shock modifies the upstream anti-sunward solar wind fluctuations as they are transmitted (propagating anti-sunward) and reflected (propagating sunward) downstream of the shock (e.g., Vainio & Schlickeiser 1998, 1999). If a medium is stationary, a wave propagates conserving its frequency. In the shock frame, the fluid structure is quasi-stationary in a time scale it takes for the wave to be transported through the shock, so Alfvén waves conserve their frequency in the shock frame. Another boundary condition at the shock for the wave vector comes from the conservation of the tangential wave length. Thus, for a transmitted, outward propagating Alfvén wave,

$$k_{1,n}(u_{1,n} - v_{a1,n}) = k_{2,n}(u_{2,n} - v_{a2,n}) \quad (11)$$

$$k_{1,t} = k_{2,t} \quad (12)$$

where $\mathbf{u}$ is the fluid velocity in the shock frame, $\mathbf{k}$ is the wave vector, $\mathbf{v}_a$ is the Alfvén velocity, subscripts 1 & 2 denote the upstream and downstream regions, and subscipts n and t denote the normal and tangential components of the vector quantities in relation to the shock surface normal. As the normal component of the magnetic field is conserved at the shock, $v_{a2,n} = v_{a1,n}/\sqrt{X}$, where $X = \rho_2/\rho_1 = u_{1,n}/u_{2,n}$ is the compression ratio of the

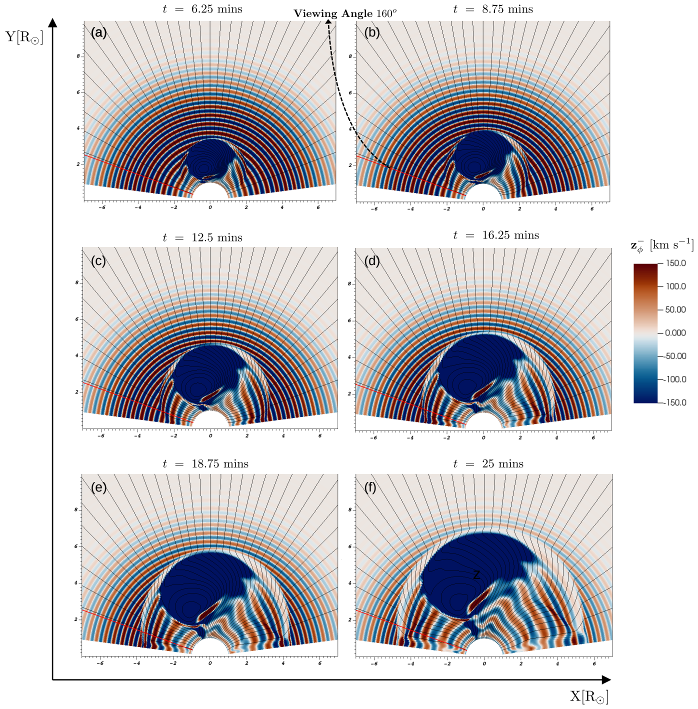

Fig. 5. Snapshots of Elsässer variables. The figure presents the anti-sunward propagating Elsässer variable $z_\phi^- = v_\phi - B_\phi/\sqrt{\mu_0\rho}$ during the CME evolution are shown at various times. The figures are annotated with a viewing angle of 160° corresponding to the CME flank.

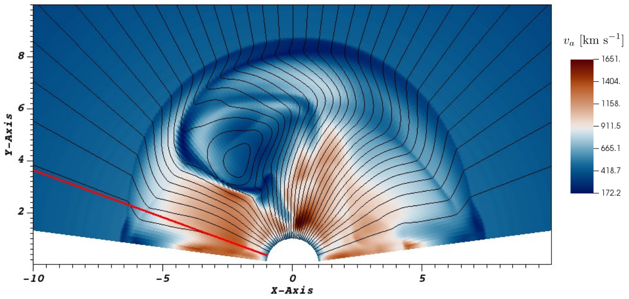

Fig. 6. Snapshot of Alfvén velocity. The Alfvén velocity, defined as $v_a = \mathbf{v_a}\cdot\hat{\mathbf{b}}$ is presented at $t = 37.5$ mins. The figure is annotated to show the CME flank at the viewing angle 160°.

shock. Thus, the downstream wave number

$$k_{2,n} = k_{1,n}X\frac{M_A - 1}{M_A - \sqrt{X}}, \tag{13}$$

where $M_A = u_{1,n}/v_{a1,n}$ is the Alfvénic Mach number, showing that the wavelength in the shock normal direction is compressed by a factor exceeding the gas compression ratio of the shock. For a low-Mach-number ($M_A \lesssim 2$) quasi-parallel fast-mode shock propagating in a low-β plasma, the compression ratio is approximately $X \lesssim M_A^2$ (Vainio & Schlickeiser 1999), implying that the wave compression can be very significant. Note that at the limit of a switch-on shock ($X = M_A^2$), wave compression becomes infinite. For a reflected wave (i.e., the case where the downstream wave is propagating towards the Sun), the wave compression is less significant,

$$k_{2,n} = k_{1,n}X\frac{M_A - 1}{M_A + \sqrt{X}}, \tag{14}$$

in particular for a low-Mach-number shock. Thus, we expect the upstream Alfvén wave to significantly decrease in wavelength as it propagates downstream of the CME shock. Therefore, the expected composition of the downstream anti-sunward solar wind fluctuations as a consequence of the shock transmission consists of a high wavelength component as the CME flank drags the waves that were transmitted downstream through the early quasi-perpendicular phase of the shock on a given field line (k_t is conserved) and a low wavelength component due to the Alfvén wave transmission across the quasi-parallel part of the shock. The waves transmitted in the early quasi-perpendicular stage (Figure 5) have a large wavelength as they experience a higher Alfvén velocity downstream of the CME shock (Figure 6) causing the increase in wavelength.

3.1.2. Fluctuations around the CME shock

In Figure 3, we observe the presence of a variety of radial (via the shock propagation) and non-radial (in the sheath plasma) enhancements in the velocity. In Figure 7, we attempt to exclude the radial flow by viewing the Elsässer variables in the frame of reference of the shock. The CME shock is detected by locating a jump in density compression that exceeds a factor of 2 and is always placed at the $x = 0$ coordinate with the Elsässer variables shown in a neighbourhood of 5 $R_\odot$. The positive x-axis values are upstream of the shock, and the negative x-axis denotes downstream.

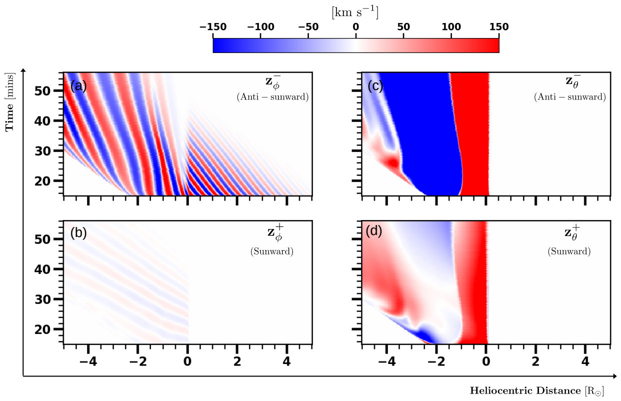

Fig. 7. Evolution of the Elsässer variables at the CME flank. The spatio-temporal evolution of the Elsässer variables for the non-radial directions in the frame of reference of the shock ($x = 0$) is presented. The quantities are shown for a viewing angle of 160°, and an Alfvénic fluctuation frequency of 3 mHz. The x-axis denotes the shock neighbourhood in units of $R_\odot$ with positive values indicating the solar wind and negative values indicating the region downstream of the shock.

In Figure 7 we present the sunward ($z_{\phi,\theta}^+$) and anti-sunward Elsässer variables for a viewing angle of 160° (CME flank) and the Alfvén wave with frequency 3 mHz injected in the quiet solar wind. The x-axis represents the distance along the given viewing angle, and the y-axis is the simulation time. The magnitude of the Elsässer variables are described using the colour intensity. In Figures 7(a), the upstream solar wind fluctuations can be observed as they are incident onto the CME shock from $x > 0$. The upstream Alfvén waves in the simulation have significant amplitudes until ≈ 10 R$_\odot$ and therefore appear to disappear beyond t ≈ 40 mins. Further into the downstream $x < 0$ we see the high wavelength component as the CME propagation modifies the downstream waves. The 'white' region between these two regions is where the shock-transmitted waves' low wavelength component should be present as expected based on the analysis in Section 3.1.1. This 'white' region corresponds to a similar region in Figures 5(e)-(f) around the CME shock where the upstream waves should be compressed. Additionally, we see the generation of sunward fluctuations in Figure 7(b) due to the interaction of solar wind fluctuations with the CME shock (Equation 14). In the θ direction, we do not see any fluctuations upstream as expected in Figure 4(d). However, in the shock neighbourhood, we can see the effect of non-radial flows due to it being a non-radial shock which was also seen in Figure 7(d).

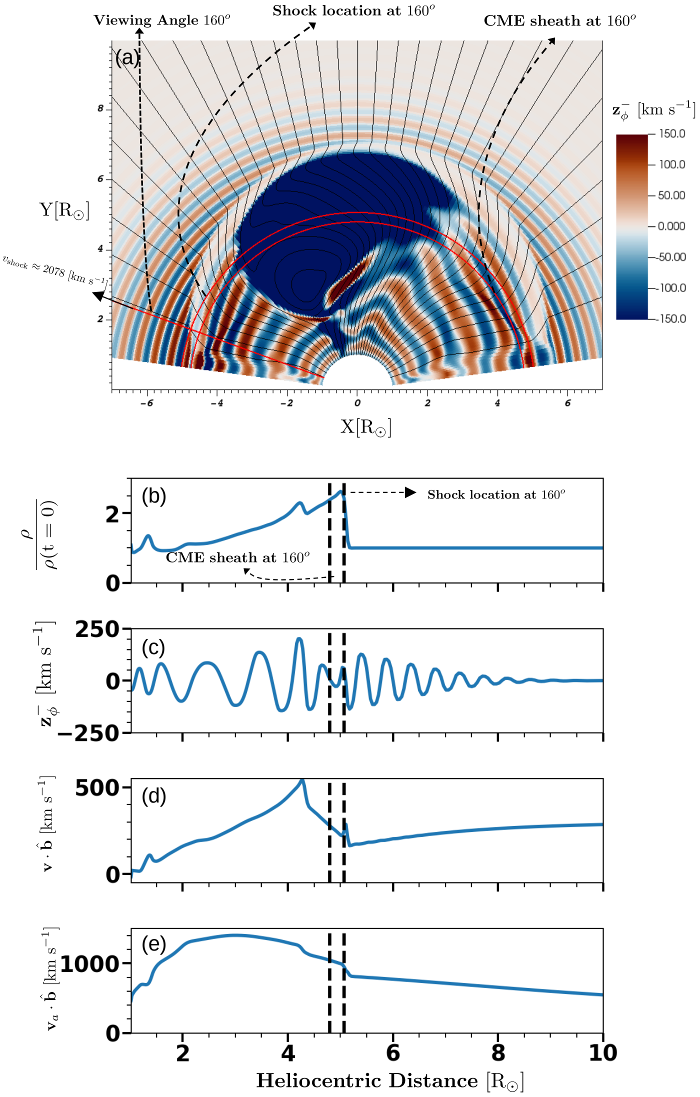

Fig. 8. Shock at the CME flank. Here we present (a) a simulation snapshot at t = 25 mins of the anti-sunward Elsässer variable z_ϕ^- with annotations describing the viewing angle along 160°, the shock location, the approximate beginning of the CME sheath, and the approximate shock velocity $v_{\rm shock}$. In (b) and (c), we present the density compression and z_ϕ^- along the viewing angle, respectively. Panels (d) and (e) present the fluid velocity and Alfvén speed along the direction of the background magnetic field.

The 'white' region in Figure 7(a) is further investigated through Figure 8 where the density compression, the anti-sunward Elsässer variable, the flow speed ($\mathbf{v} \cdot \mathbf{b}$), and the Alfvén speed along the background field ($\mathbf{v}_a \cdot \mathbf{b}$) are presented at t = 25 mins. Panel (a) of the figure is an annotation of Figure 5(f) with the location of the CME shock and the approximate beginning of the sheath, where we start observing the large wavelength fluctuations. The 'white' region thus corresponds to the location between these two markers. Panel (b) shows the density compression utilised in identifying the shock, and panel (c) is the anti-sunward Elsässer variable. The average shock velocity at the 160° viewing angle between t = 6.25 mins to t = 31.25 mins is found to be ≈ 2078 km s^{-1} as annotated in panel (a). The shock is associated with a gas compression ratio of ≈ 2 (panel (d)), with the Alfvén speed increasing from upstream to downstream (panel (e)). Then, through Equation 14 the wavelength of the upstream wave would be compressed by about three times downstream of the shock. The absence of the anticipated compression of the upstream Alfvén wave in our simulation indicates that the spatial grid does not adequately resolve this specific region. This causes the transmitted waves to be of lower amplitude in this location, as observed in panel (c), signifying numerical dissipation. Therefore, the downstream fluctuations plotted in Figure 7 don't contain the additional shock compressed Alfvén waves. However, the restricted grid resolution for this simulation is necessary to sustain a monochromatic Alfvén wave before the CME injection by numerically damping the waves before their decay. In appendix A we present a modified simulation where the shock-compressed waves are captured. The results in the appendix show an adherence to the expected composition of the downstream waves as per Section 3.1.2, with the downstream waves becoming modified compared to Figure 7 only after t ≈ 20 mins due to possible wave steepening. Thus, in practise the downstream solar wind fluctuations would contain high and low-wavelength components due to the CME passage and upstream waves transmission respectively, prior to the development of further non-linear interactions.

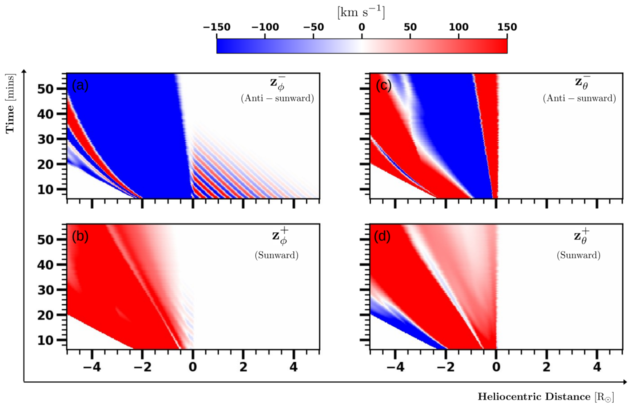

Fig. 9. Evolution of the Elsässer variables at the CME nose. Similar plot as Figure 7 except with a viewing angle of 105°. The x-axis similarly denotes the shock neighbourhood in units of $R_\odot$ with the shock centred at x = 0.

In Figure 9, we show the solar wind fluctuations around the shock when viewing the CME head-on instead of the flank. Panel (a) shows the upstream solar wind fluctuations incident onto the shock. A similar 'white' region corresponds to the region where the incident waves would be compressed. However, in the far downstream region $x < 0$, we only observe large non-radial flows as the large positive guide field B_ϕ of the flux-rope affects the surrounding plasma to generate a non-radial flow. These non-radial flows are additionally observed in the sunward component (panel (b)). In the θ directions (panels (c) and (d)), the large flows are generated due to the non-radial topology of the CME shock.

Therefore, a primary difference between solar wind fluctuations downstream of the CME shock for a head-on encounter (Figure 9) compared to a flank encounter (Figure 7) is the absence of large-wavelength amplified fluctuations which are comparable in size to the non-radial flows. Through Figure 8(a) it is seen that the CME shock is non-radial as the shock velocity is greater head-on (the direction where the FR is expanding) than at the flank. This indicates that the wavelength of the shock-compressed upstream waves differ as the compression depends on the Alfvén mach number in the shock frame of reference. Furthermore, as the shock expands faster than the ambient Alfvén speed we would expect different characteristics of the fluctuations closer to the shock (containing a mix of shock-transmitted and already present fluctuations) and further downstream (with the CME-amplified fluctuations).

4. Formation of the CME Sheath

In Section 3, we discussed the dependence of the CME sheath fluctuations on the upstream solar wind conditions and the shock properties. The interaction of the solar wind fluctuations with the CME shock gave rise to both sunward and anit-sunward Alfvénic fluctuations at the CME flank (Figures 7), along with the compression of anti-sunward upstream waves. In addition, the CME sheath contains non-radial flows due to the magnetic structure of the FR and the non-radial CME shock (Figures 4(c)- 4(d)). The extent of the non-radial flows, represented by the dark blue region in Figure 4(c) and Figure 5, suggests that their spatial extent is comparable to the Alfvén waves at the CME flanks. This limitation could hinder the presence of large-amplitude Alfvénic fluctuations in the presence of similarly large non-radial flows. Thus, we now investigate the influence of the Alfvén waves on the growth of the CME sheath region and propagation of the CME shock. This allows us to understand the effect of Alfvén waves on the shock properties and infer the development of non-radial flows as the CME propagates further in the solar wind.

Previous studies have shown significant variations of the sheath thickness based on the physical properties of the CME, more precisely the properties of the CME flux rope (FR), and the shock compression ratio (Russell & Mulligan 2002). Thus, we investigate how the large-scale structure of the sheath depends on the density and injection velocity of the FR driving it, and the frequency of the Alfvénic fluctuations that are present in the solar wind. These different cases, studied by varying a selection of the parameter values of the simulation setup, including the case studied in previous sections (henceforth designated as C1) are detailed in Table 1.

We find that the large-scale structures of the sheath, such as a PUC region, high-speed flows, and magnetic field line draping are similar for all the cases considered in Table 1.

To quantify the differences, for each model run, the extent of the sheath, location of the FR, and the shock location for a viewing angle of 105° (head-on encounter) are computed and presented in Figure 10(a)-(c) as a function of time. The computation of the shock's location relies on the density compression ratio, while the positioning of the flux rope (FR) is determined by identifying the first closed magnetic field contour encountered along the viewing angle directed towards the Sun. Subsequently, in Figures 10(d)-(i), we display the snapshot of the simulation for the various cases (Table 1) at $t = 21$ mins from the event onset. These snapshots are overlaid with markers displaying the viewing angle, shock location, and the FR leading edge location.

Case	**CME Parameters**		**$f_{\rm inj}$ [mHz]**
	$\mathbf{v}_{\rm ej}$ [km s^{-1}]	$\rho(t=0)/\rho_0$	
C1	500	1	3
C2	500	2	3
C3	500	0.5	3
C4	1000	1	3
C5	500	1	5
C6	500	1	0

Table 1. Model parameters used in the different simulation runs. The ejection velocity $\mathbf{v}_{\rm ej}$ is the initial velocity imparted to the CME along 90°, and the ρ/ρ_0 parameter is the density imparted to the CME as a multiple of the low-coronal boundary density, and $f_{\rm inj}$ denotes the frequency of the injected Alfvénic perturbations.

Panels (b) and (c) in Figure 10 show that the lower the density of the FR, the faster the FR and its leading shock propagate through the corona, i.e. this is seen by comparing the high-density (C2; blue curve), nominal density (C1; black curve) and the low-density (C3; orange curve) cases. Note that for these three cases the initial FR speed and the frequency of injected fluctuations were the same (500 km s^{-1} and 3 mHz, respectively). From these cases, the low-density FR (C3) that propagates fastest through the solar corona has the widest sheath (panel a). This dependency of the propagation speed on density can be understood by considering the deflection of case C3 (as explained in Section 3 deflection is expected to result from magnetic reconnection at the FR boundaries). The comparison between simulation snapshots in Figures 10(d)-(f) show that the low-density case C3 deflects more than the higher density cases C1 and C2. This deflection causes our selected viewing angle to probe more the flank of the CME for C3, while for C1 and C2 their higher inertia prevents them deflecting and they are probed head-on as intended.

Next we explore the effect of FR injection velocity. The shock and the FR for C4 (green curve) propagate faster through the corona when compared to C1 that has the same density but slower speed see Figure 10(b), Figure 10 (c)). This results to a much smaller sheath thickness for C4 than for C1 (Figure 10(a)). Finally, when we increase the Alfvénic fluctuation frequency in C5, and compare to run C1 that has otherwise identical parameters, there is no notable difference in the FR location (Figure 10(b)), but the shock propagates faster (Figure 10(c)) causing the sheath extent to increase (Figure 10(a)). Moreover, when not injecting any Alfvénic fluctuations as is the case for run C6, we still see no difference in the FR location compared to C1, but the shock propagates slower and the sheath extent decreases.

The variations in the shock evolution (Figure 10(c)) for the different cases can be understood through steepening of MHD waves. The initial eruption of the CME onto a quasi-steady solar wind generates a fast wave propagating ahead of the CME as it initially strongly expands in the surrounding plasma. If we assume the wave driven by the FR to be a pressure wave, then as this wave propagates it locally compresses the plasma and increases the local sound speed. This would cause the next pressure wave pulse generated by the outward propagating FR to catch up to the preceding wave modes, thus causing a shock to be generated by the steepening of large-amplitude compressive disturbances. In the general case, the fast wave generated by the

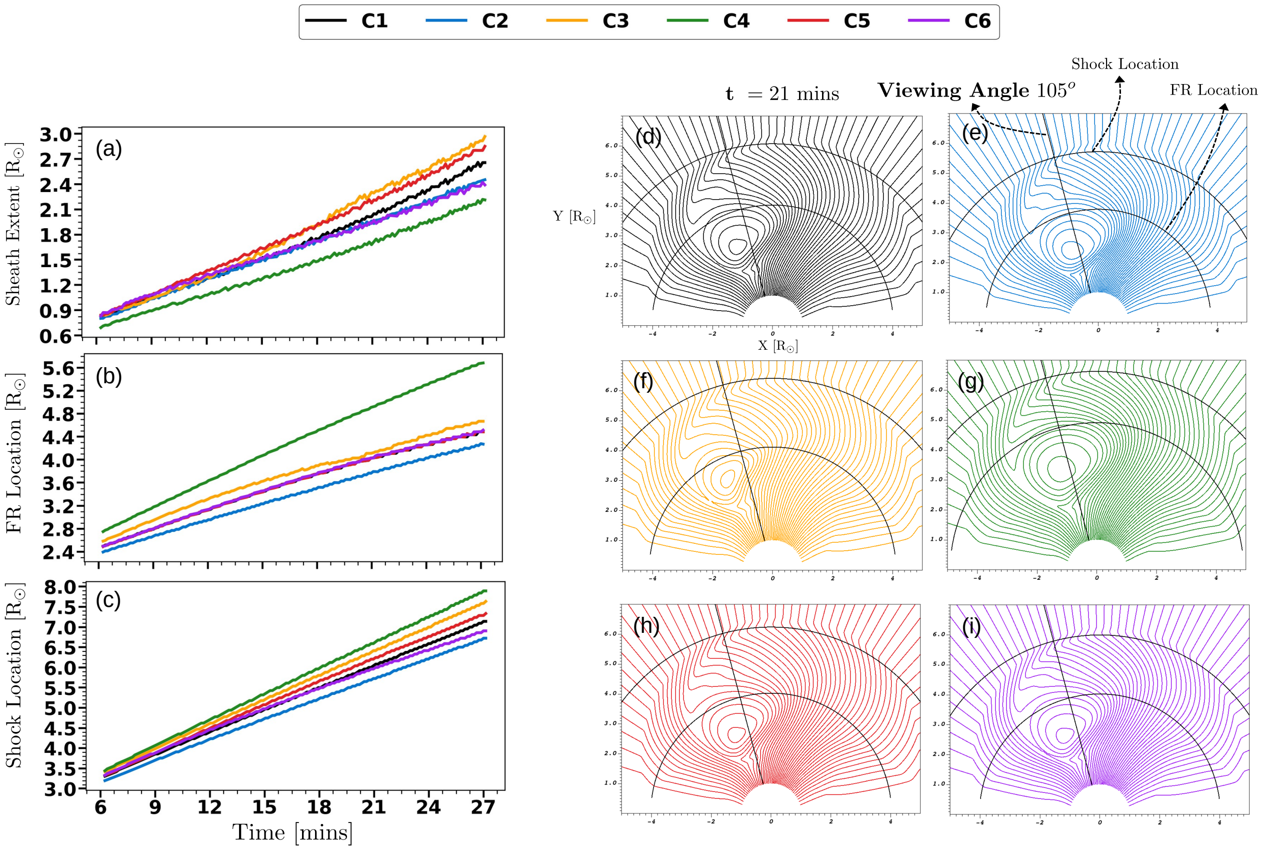

Fig. 10. Formation of the CME sheath in the different simulation runs. The evolution of the (a) radial extent of the sheath, (b) flux rope leading edge, and (c) location of the CME shock along a viewing angle of 105° for the simulation runs detailed in Table 1. The individual runs at time $t = 21$ mins are visualised in (d)-(i) with the magnetic field lines coloured based on the case number. Additionally, in each panel (d)-(i), the viewing angle, the flux rope, and shock locations are indicated.

FR eruption would be an MHD wave. The rate of steepening a fast mode MHD wave, with no additional assumptions other than the compressibility of the medium, has been previously derived (e.g., Kantrowitz et al. 1966) to be given by

$$\gamma_s = \omega \frac{\delta\rho}{\rho}\left[1 + \frac{1}{2}\frac{(\gamma-1)v_A^2 c_s^2 \sin^2\theta + (v_{\rm ph}^2 - c_s^2)^2}{v_A^2 c_s^2 \sin^2\theta + (v_{\rm ph}^2 + c_s^2)^2}\right] \tag{15}$$

Here ω is the wave frequency, v_A the Alfvén speed, c_s the sound speed, v_{ph} the phase speed of the wave, and θ is the wave normal angle relative to the magnetic field. The steepening rate depends primarily on the compressibility of the medium ($\delta\rho/\rho$) where ρ corresponds to the undisturbed solar wind density, with minor contributions from the term in the brackets (Kennel et al. 1985; Tsurutani et al. 1987). Among the CME runs described in Table 1, the high-density FR (case C2) corresponds to an increased $\delta\rho/\rho$, while for the low-density FR (case C3) $\delta\rho/\rho$ is smaller than for C1. As a consequence, for C2 the wave steepens to a shock faster (at a lower starting height) than for C1, while for C3 the shock forms later. The shock locations in Figure 10(c) grow linearly with time which indicates that after the fast wave steepens, the shock propagates with a constant velocity in this region. Therefore, for the case of C2 the fast wave steepens to a shock fastest from the investigated cases and the shock thus forms at the lowest heights in the corona (Figure 10(c)). For C3 in turn, the wave decelerates slower and the shock forms at a relatively higher height.

For run C4 the higher injection velocity does not have a direct influence on the steepening rate (Equation 15), i.e. the shock starts at approximately at similar height in Figure 10(c) as for C1. However, because the FR in C4 propagates much faster through the corona than for C1 (due to the higher injection velocity), it drives the shock faster at the CME nose. So, the difference in the shock location between C4 and C1 increases as the simulation progresses. Finally, the cases C5 and C6 show that the frequency of the upstream Alfvénic perturbations seem to affect the speed of the CME shock. We note that this dependence of the shock speed on the Alfvén wave frequency is independent of the grid resolution (appendix A). In Section 2.1, we showed that Alfvénic waves in the solar wind in our simulation could not steepen to form shocks themselves. Only the interaction of the Alfvén waves with the shock, and the initially propagating fast MHD wave prior to shock formation may alter the shock speed. It is to be noted that this effect of the Alfvén wave frequency affecting the shock formation is shown for a quasi-parallel shock in this simulation. In the case of a perpendicular shock, previous studies (Lu et al. 2009) have only indicated structural modifications at the shock front without an influence on the propagation speed.

Thus, the propagation velocity of the CME shock depends initially on the effect of the wave steepening followed by the FR driving it further. The FR itself propagates based on the injection velocity and momentum contributing to the resulting force imbalance at onset. This variation of how different parameters affect the shock and FR location separately causes differences in the CME sheath extent.

5. Conclusion

This study presents the interaction between small amplitude Alfvénic fluctuations and a CME in the low corona using 2.5D time-dependent MHD simulation. The fluctuations in the quasi-steady solar wind are linearly-polarised and monochromatic in frequency. They are injected using time-dependent boundary conditions in the low corona.

In Section 2.1, we described the linear evolution of the injected Alfvén waves without decaying into compressive and reflected wave modes. In this scenario, we found that the CME sheath would consist of low-wavelength waves that are compressed by the shock and high-wavelength waves transmitted in the initial quasi-perpendicular phase of the CME expansion, which were modified in wavelength by the CME shock passage. The Alfvén waves downstream of the CME shock were inhibited close to the FR due to non-radial flows. While this result was obtained for a 2D simulation, we can extrapolate this argument into a higher dimension. In a 3D case, we would observe non-radial flows in ϕ at the CME flanks as well (in the same manner as we do for θ). Thus, we might expect the CME sheath fluctuations to consist of low-wavelength components based on the non-radial flows present in each direction. Due to the importance of the CME sheath structure in influencing the fluctuations present in this region, we investigated the formation of the sheath in Section 4. We found the CME-driven shock to be formed due to wave steepening with an additional constraint on the frequency of the fluctuations present in the system. At the same time, the flux rope evolution is unaffected by the frequency of the fluctuations. In the discussion presented in this study, we don't address the Alfvén waves generated by the magnetic recconection (Cranmer 2018; Lynch et al. 2014) inside the CME sheath. We cannot capture these additional waves in this simulation as they require a much finer simulation grid. The properties of such reconnection-driven Alfvén waves depend on the rate of reconnection, plasma β, and magnetic field strength (Kigure et al. 2010). A complete discussion of the impact of these waves on the observed properties of fluctuations inside CME sheaths would require further study. The results presented in this study are thus in the context of the shock transmission of already-present solar wind fluctuations. Therefore, the applicability of these results is valid close to the CME shock when compared with spacecraft observations.

A primary result of this study is the transmission of the upstream Alfvén waves based on the upstream solar wind conditions in the frame of reference of the CME shock (Section 3.1.1). This transmission process naturally generates sunward propagating Alfvén waves, with the compression of the upstream anti-sunward propagating waves varying in the latitudinal direction (θ) due to the varying shock speeds. This indicates that Alfvénic fluctuations have only anti-sunward components upstream and both sunward and anti-sunward components downstream due to their interaction with the CME shock. This behaviour has been observed across CME shocks (Good et al. 2020). Additionally, the properties of the downstream Alfvénic fluctuations will depend on their relative distance to the CME shock, with locations closer to the shock containing more compressed upstream waves. This might indicate varying spectral slopes in the near-shock, mid-sheath, and near-FR regions of the CME sheath (Kilpua et al. 2020). In Section 4, we observed the Alfvén wave frequency affecting the shock velocity. This requires further study, as previous studies investigating this interaction for perpendicular shocks found no appreciable differences in shock speeds. Thus, the result presented in this study might be a feature of the quasi-parallel CME shock.

Acknowledgements. The work has been supported by the Finnish Centre of Excellence in Research on Sustainable Space (FORESAIL). This is a project under the Academy of Finland, and this research has been supported by the European Research Council (SolMAG; grant no. 724391) as well as Academy of Finland project SWATCH (343581). The authors are also grateful to the anonymous referee for their constructive input during the peer review process.

References

Asvestari, E., Pomoell, J., Kilpua, E., et al. 2021, Astronomy & Astrophysics, 652, A27
Asvestari, E., Rindlisbacher, T., Pomoell, J., & Kilpua, E. K. 2022, The Astrophysical Journal, 926, 87
Bale, S., Kellogg, P., Mozer, F., Horbury, T., & Reme, H. 2005, Physical Review Letters, 94, 215002
Belcher, J. & Davis Jr, L. 1971, Journal of Geophysical Research, 76, 3534
Belcher, J., Davis Jr, L., & Smith, E. 1969, Journal of Geophysical Research, 74, 2302
Chen, C. 2016, Journal of Plasma Physics, 82
Cohen, R. H. & Kulsrud, R. M. 1974, The Physics of Fluids, 17, 2215
Coleman Jr, P. J. 1968, The Astrophysical Journal, 153, 371
Cranmer, S. & Van Ballegooijen, A. 2005, The Astrophysical Journal Supplement Series, 156, 265
Cranmer, S. R. 2018, The Astrophysical Journal, 862, 6
D'Amicis, R. & Bruno, R. 2015, ApJ, 805, 84
Das, I., Opher, M., Evans, R., Loesch, C., & Gombosi, T. I. 2011, The Astrophysical Journal, 729, 112
Gershman, D. J., Connerney, J. E., Kotsiaros, S., et al. 2019, Geophysical Research Letters, 46, 7157
Gibson, S. & Low, B. 2000, Journal of Geophysical Research: Space Physics, 105, 18187
Gibson, S. E. & Low, B. 1998, The Astrophysical Journal, 493, 460
Goldstein, M. L. 1978, The Astrophysical Journal, 219, 700
González, C., Tenerani, A., Matteini, L., Hellinger, P., & Velli, M. 2021, The Astrophysical Journal Letters, 914, L36
Good, S., Kilpua, E., Ala-Lahti, M., et al. 2020, The Astrophysical Journal Letters, 900, L32
Good, S. W., Hatakka, L. M., Ala-Lahti, M., et al. 2022, MNRAS, 514, 2425
Hollweg, J. V. 1971, Journal of Geophysical Research, 76, 5155
Isavnin, A. 2016, The Astrophysical Journal, 833, 267
Kalliokoski, M. M., Henderson, M. G., Morley, S. K., et al. 2022, Authorea Preprints
Kalliokoski, M. M., Kilpua, E. K., Osmane, A., et al. 2020in , Copernicus GmbH, 683–701
Kantrowitz, A., Petschek, H., & Kunkel, W. 1966, McGraw-Hill Book Company, New York, 147
Kato, Y., Steiner, O., Hansteen, V., et al. 2016, The Astrophysical Journal, 827, 7
Kennel, C. F., Edmiston, J. P., & Hada, T. 1985, Washington DC American Geophysical Union Geophysical Monograph Series, 34, 1
Kigure, H., Takahashi, K., Shibata, K., Yokoyama, T., & Nozawa, S. 2010, Publications of the Astronomical Society of Japan, 62, 993
Kilpua, E., Balogh, A., Von Steiger, R., & Liu, Y. 2017a, Space Science Reviews, 212, 1271
Kilpua, E., Fontaine, D., Moissard, C., et al. 2019, Space Weather, 17, 1257
Kilpua, E., Good, S., Ala-Lahti, M., et al. 2021, Frontiers in Astronomy and Space Sciences, 7, 610278
Kilpua, E., Hietala, H., Koskinen, H., Fontaine, D., & Turc, L. 2013in , Copernicus Publications Göttingen, Germany, 1559–1567
Kilpua, E., Hietala, H., Turner, D., et al. 2015, Geophysical Research Letters, 42, 3076
Kilpua, E., Koskinen, H. E., & Pulkkinen, T. I. 2017b, Living Reviews in Solar Physics, 14, 1

Kilpua, E. K., Fontaine, D., Good, S. W., et al. 2020in , Copernicus GmbH, 999–1017

Kilpua, E. K. J., Good, S. W., Dresing, N., et al. 2021, A&A, 656, A8

Kissmann, R. & Pomoell, J. 2012, SIAM Journal on Scientific Computing, 34, A763

Koskinen, H. 2011, Physics of space storms: From the solar surface to the Earth (Springer Science & Business Media)

Lu, Q., Hu, Q., & Zank, G. P. 2009, The Astrophysical Journal, 706, 687

Lynch, B., Edmondson, J., & Li, Y. 2014, Coronal Magnetometry, 421

Matthaeus, W., Ambrosiano, J., & Goldstein, M. L. 1984, Physical review letters, 53, 1449

Mikić, Z., Downs, C., Linker, J. A., et al. 2018, Nature Astronomy, 2, 913

Moissard, C., Fontaine, D., & Savoini, P. 2019, Journal of Geophysical Research: Space Physics, 124, 8208

Nakariakov, V., Roberts, B., & Murawski, K. 1997, Solar Physics, 175, 93

Perez, J. C. & Chandran, B. D. 2013, The Astrophysical Journal, 776, 124

Pomoell, J., Aran, A., Jacobs, C., et al. 2015, Journal of Space Weather and Space Climate, 5, A12

Pomoell, J., Aran, A., Jacobs, C., et al. 2015, Journal of Space Weather and Space Climate, 5, A12

Pomoell, J. & Vainio, R. 2012, The Astrophysical Journal, 745, 151

Ruohotie, J., Kilpua, E. K. J., Good, S. W., & Ala-Lahti, M. 2022, Frontiers in Astronomy and Space Sciences, 9, 943247

Russell, C. & Mulligan, T. 2002, Planetary and Space Science, 50, 527, solar System Magnetosheaths-A Special Issue in Honor of John Spreiter

Schekochihin, A., Cowley, S., Dorland, W., et al. 2009, The Astrophysical Journal Supplement Series, 182, 310

Siscoe, G. & Odstrcil, D. 2008, Journal of Geophysical Research: Space Physics, 113

Sishtla, C. P., Pomoell, J., Kilpua, E., et al. 2022, Astronomy & Astrophysics, 661, A58

Soljento, J. E., Good, S. W., Osmane, A., & Kilpua, E. K. 2023, The Astrophysical Journal Letters, 946, L19

Solov'ev, L. 1968, Sov. Phys. JETP, 26, 400

Tomczyk, S., McIntosh, S., Keil, S., et al. 2007, Science, 317, 1192

Tsurutani, B. T., Thorne, R. M., Smith, E. J., Gosling, J., & Matsumoto, H. 1987, Journal of Geophysical Research: Space Physics, 92, 11074

Tu, C.-Y. & Marsch, E. 1995, Space Science Reviews, 73, 1

Vainio, R. & Schlickeiser, R. 1998, Astronomy and Astrophysics, 331, 793

Vainio, R. & Schlickeiser, R. 1999, Astronomy and Astrophysics, v. 343, p. 303-311 (1999), 343, 303

Van Ballegooijen, A., Asgari-Targhi, M., Cranmer, S., & DeLuca, E. 2011, The Astrophysical Journal, 736, 3

Verbeke, C., Pomoell, J., & Poedts, S. 2019, A&A, 627, A111

Verdini, A. & Velli, M. 2007, The Astrophysical Journal, 662, 669

Zank, G. & Matthaeus, W. 1992, Journal of plasma physics, 48, 85

Appendix A: Shock compressed Alfvén waves

In this appendix we present a modified simulation of the nominal run (case C1 in Table 1) discussed in Section 3 where we improve the resolution between 1.1 $R_\odot$ to 10 $R_\odot$ to capture the compression of upstream Alfvén waves due to the shock that are not resolved in Section 3.1.1. Here we detail the methodology for introducing the modified resolution, and report the expected propagation of Alfvén waves based on the discussion presented in Section 3. Therefore, the results presented in this appendix validate the approach presented in this manuscript where we utilise a reduced simulation resolution while still obtaining the proper physics.

Appendix A.1: Modifying the grid resolution

As described in Section 2, the simulation is performed in three steps:

1. Generating a steady-state solar wind solution without fluctuations.
2. Generating a quasi-steady state wind by injecting Alfvén waves.
3. Introducing the CME.

A reduced resolution with 500 grid cells logarithmically spaced in the radial direction results in numerical damping of the Alfvén waves in the corona and inhibit the generation of density fluctuations and alternate Alfvén wave modes (Section 2.1). Thus, after obtaining a quasi-steady wind with a reduced resolution, we modify the simulation grid to have 4000 equally spaced cells between 1.1 $R_\odot$ to 10 $R_\odot$ solar radii while preserving the original grid below 1.1 $R_\odot$ and beyond 10 $R_\odot$. This higher resolution in the region of interest where the Alfvén waves are present in the simulation enables us to capture the compression at the CME shock. The choice of 4000 cells was made after noting that the solar wind behaviour is unchanged for 3000 and 3500 grid cells as well.

Figure A.1 illustrates the effect of the modified grid on the Alfvén wave transmission by presenting a figure similar to Figure 8. In panels (a), (c) we observe that Alfvén waves seen as crests and troughs of the z_ϕ^- Elsässer variable are of a higher amplitude than in Figure 8 due to a lower level of numerical damping. However, the CME shock and the start of the long-wavelength CME sheath region is seen to occur at the same location as in the lower resolution simulation as annotated in the figure. The primary difference between Figure A.1 and Figure 8 is the shock compressed region in panel (c) between the vertical annotations. In this region we observe the upstream waves compressed in frequency (as described in Section 3.1.1), with the modified grid capturing one wavelength of this compressed Alfvén wave. However, after this compressed region the Alfvén waves observed further downstream are similarly of longer wavelength as in the lower resolution runs as the Alfvén speed increases again. To verify if the grid resolution captures the entire compressed wave, we plot the flow speed ($\mathbf{v}\cdot\hat{\mathbf{b}}$), and the Alfvén speed along the background field ($\mathbf{v}_a \cdot \hat{\mathbf{b}}$) in Figure A.1(d), (e). Assuming the shock normal to be exactly in the direction of the upstream magnetic field (in the radial direction), and by estimating the shock speed between t = 6.25 mins to t = 31.25 mins as $\approx$ 2087 km s^{-1} we obtain the Alfvén mach number in the shock frame to be $\approx$ 2.45 and $\approx$ 1.78 in the upstream and downstream respectively. Additionally, taking the gas compression ratio to be $\approx$ 2 (panel (d)), we can estimate the downstream wavelength (Equation 13) to be three times smaller than the upstream wavelength which can be resolved by the higher-resolution grid. It is to be noted that the average shock velocity with the modified grid ($v_{\rm shock}$ $\approx$ 2087 km s^{-1}) is marginally higher than for the original grid ($v_{\rm shock}$ $\approx$ 2078 km s^{-1}) possibly due to the modified grid better resolving the interactions of the wave with the shock.

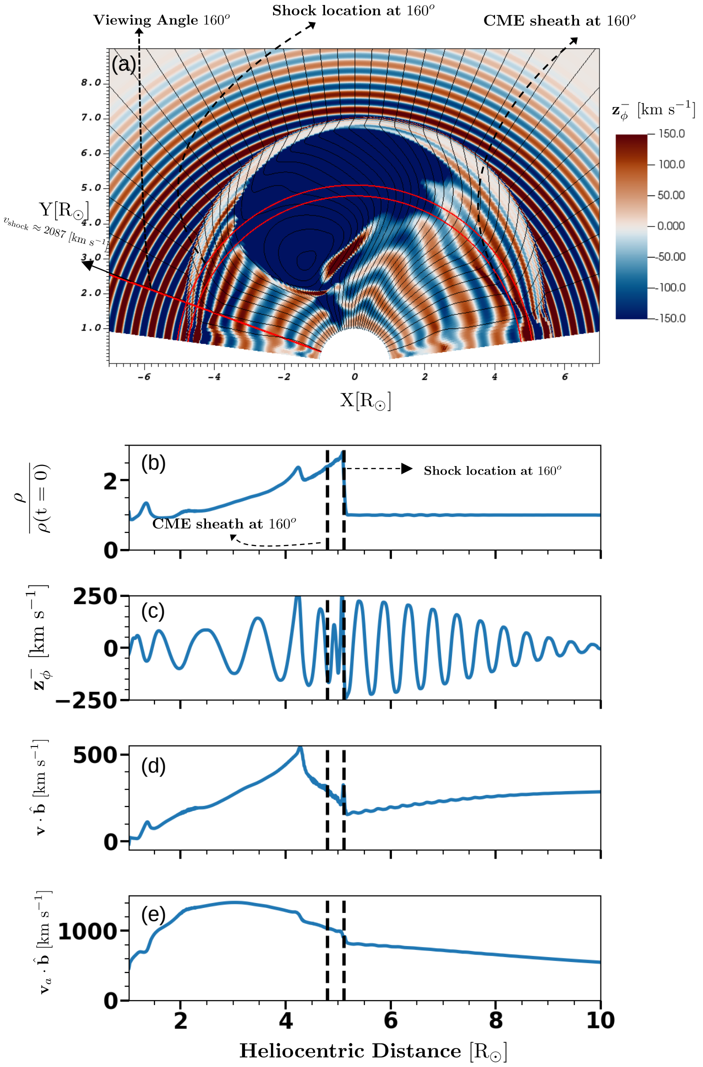

Fig. A.1. Shock at the CME flank for the modified resolution simulation run. Here we present a figure similar to Figure 8 except with a modified grid (higher resolution) between 1.1 $R_\odot$ to 10 $R_\odot$. The plot shows (a) a simulation snapshot at t = 25 mins of the anti-sunward Elsässer variable $\mathbf{z}_\phi^-$ with annotations describing the viewing angle along 160°, the shock location, the approximate beginning of the CME sheath, and the approximate shock velocity $v_{\rm shock}$. In (b) and (c), we present the density compression and $\mathbf{z}_\phi^-$ along the viewing angle, respectively. Panels (d) and (e) present the fluid velocity and Alfvén speed along the direction of the background magnetic field.

Finally, the effect of the Alfvén waves on the propagation of the CME is discussed in Section 4. The flux-rope propagates based on it's force imbalance, and did not present a significant dependence on the Alfvén wave frequency. In contrast, the shock velocity increased with the wave frequency. To verify whether such a result is dependant on the grid resolution we performed a similar analysis as in Section 4 to check the nominal case C1 against the simulation with the modified resolution as in the appendix. The results showed that the Alfvén wave has no further effect on the CME shock velocity with the increased resolution.

Appendix A.2: Alfvén wave transmission across the shock

The transmission of the upstream Alfvén wave occurs based on the gas compression ratio across the shock and the upstream Alfvén mach number in the shock frame. To illustrate the compressed wave further, we show Figures A.2 and A.3 which are similar to Figure 7 but use the modified high-resolution grid, and are presented for viewing angles of 160°, and 105°.

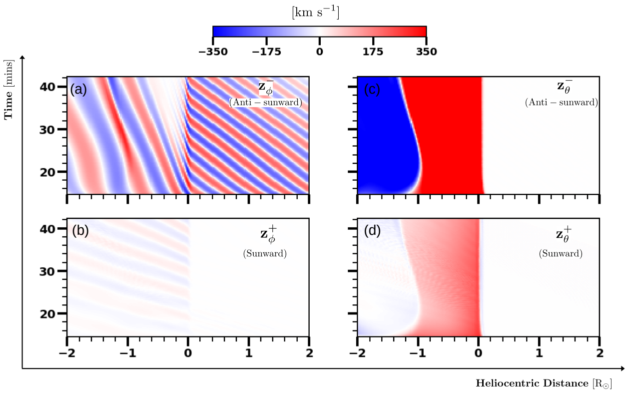

Fig. A.2. Evolution of the Elsässer variables at the CME flank for the modified simulation grid. A similar plot as Figure 7 except using a modified grid (higher resolution) between 1.1 $R_\odot$ to 10 $R_\odot$. The x-axis similarly denotes the shock neighbourhood in units of $R_\odot$ with the shock centred at $x = 0$.

In Figure A.2 (comparable to Figure 7) we see the upstream waves in panel (a) incident to the shock with the far downstream region ($x < 0$) showing the large wavelength Alfvén waves. The downstream region also shows an enhancement of the Alfvén wave amplitudes beyond t = 20 mins. We now also observe the compressed waves near the shock which are amplified but quickly dissipate as the shock propagates further. This dissipation and subsequent enhancement of the downstream waves seems to indicate steepening of the compressed waves. The Elsässer variables in θ remains as presented in Section 3.1.2.

For a viewing angle of 105° (CME head-on) in Figure A.3 we see a similar compression of the upstream waves and subsequent dissipation as the shock progresses further. The far downstream region shows the expected large flow due to the presence of the flux-rope magnetic field. The panels (b), (c), (d) have similar behaviour as in Figure 9.

Therefore, the upstream Alfvén waves are compressed by the CME shock and further interact non-linearly with each other to dissipate and steepen the downstream waves. The high-resolution grid captures the expected behaviour of the waves as described in Section 3.1.1 with an additional effect based on the wave dissipation as the CME propagates beyond 10 R$_\odot$. The resolution does not appear to have any effect on the CME dynamics.

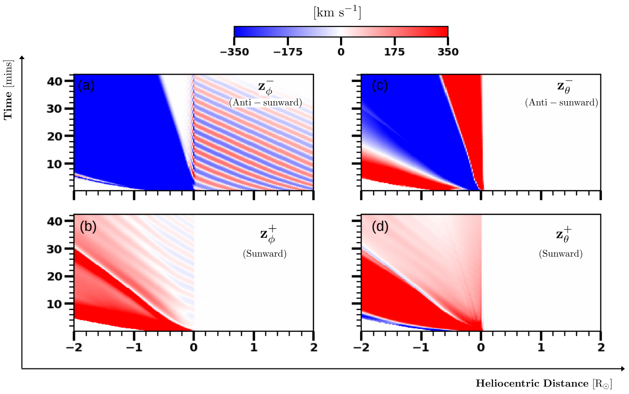

Fig. A.3. Evolution of the Elsässer variables at the CME nose for the modified simulation grid. A similar plot as Figure A.2 except with a viewing angle of 105°. The x-axis similarly denotes the shock neighbourhood in units of $R_\odot$ with the shock centred at $x = 0$.